Vol. 47, No. 4 (2025) 718-731, DOI: 10.24874/ti.2011.08.25.09

Tribology in Industry

www.tribology.rs

RESEARCH

Fullerene C60 Versus Synthetic Based Oils on Compression Piston Ring Tribology

Elias Tsakiridis[a], Pantelis Nikolakopoulos[a,*]

[a]*Machine Design Laboratory, Mechanical Engineering and Aeronautics Department, University of Patras, Greece.*

Keywords:

Lubricant
C60 fullerene
Cavitation
Viscosity
Piston ring tribology

* Corresponding author:

Pantelis Nikolakopoulos
E-mail: pnikolakop@upatras.gr

Received: 20 June 2025
Revised: 8 August 2025
Accepted: 3 October 2025

A B S T R A C T

This study examines the effectiveness of C60 fullerenes as additives to improve lubricant performance in piston ring–cylinder liner tribological systems. Viscosity measurements of synthetic and fullerene-based oils were performed using a capillary tube viscometer under varying temperature and pressure. The data were incorporated into a CFD model of compression piston ring to assess friction, cavitation, and hydrodynamic pressure. Cavitation effects were also investigated and commented on. Results show that fullerene-enhanced lubricants retain higher viscosity at elevated temperatures and reduce friction force, enhancing engine efficiency and emission characteristics.

1. INTRODUCTION

The pursuit of enhanced engine efficiency has driven a reduction in lubricating oil viscosity, aimed at minimizing losses within hydrodynamic lubrication mechanisms. This approach has, in turn, elevated the significance of piston ring and cylinder bore systems in managing mixed and boundary lubrication scenarios. To optimize friction efficiency in certain lubrication regimes, one of the strategies involves the application of friction modifiers [1,2].

Synthetic lubricants frequently incorporate nanoparticles as additives, which come in varying dimensions, forms, and volume ratios. In numerous tribological applications, lubricants enriched with nanoparticles have demonstrated superior performance in terms of reducing friction and wear. This improvement can be attributed to their exceptional dispersion properties, enhanced lubricating characteristics, and improved thermal conductivity.

Consequently, gaining a comprehensive understanding of nanoparticle behavior is imperative for advancing mechanisms of lubrication, which, in its turn, can aid in meeting stringent regulations governing vehicle emissions [1]. The increasing significance of tribofilm formation is underscored by its initiation through the action of friction modifiers and antiwear additives at the contact interface. This effect proves especially advantageous in mitigating frictional losses and reducing energy consumption, particularly within the realm of transportation. Notably, these advantages become most apparent in situations where the oil film is limited, as in mixed and boundary lubrication scenarios [2]. To attain reduced friction and wear in various mechanical interactions, a variety of nanoparticle types, typically ranging from 1 to 120 nanometers in size, are introduced into diverse lubricants.

In the piston ring- cylinder liner conjunction where the lubricant flows in mixed lubrication regime, it is crucial to investigate how both friction and wear can be minimized. Using fullerene enhanced lubricants is of great interest, as previous works highlight their great significance in improving engine's performance [3]. Viscosity is one of the primary factors in lubricant selection. In the case of a low viscosity, the lubricant film would not reach the expected or desired thickness, and on the other hand, if the viscosity is higher than the requested value, it impedes motion by increasing resistance. However, viscosity is not a steady-state property, as it takes different values according to temperature and pressure as well. In this research the viscosity of the monograde lubricant SAE 30 and one using fullerenes as additives is investigated and computed experimentally. The viscosity measurement tests were performed using an EH105 capillary tube viscometer manufactured by DELTALAB.

Temperature plays a vital role in viscosity, affecting its values [4]. It is crucial to model the viscosity depending on the temperature in the CFD model, as described by Zavos and Nikolakopoulos [5]. The fullerene particles affect the performance of the lubricant, not only in terms of viscosity, but also in terms of friction. The friction force is calculated considering the presence of asperities. The rough surfaces are modelled considering the stochastic Greenwood-Tripp model [6].

The lubricant flow is modelled as per [7,8], considering the geometry of the ring and the mathematical equations used to compute the parameters of the model. Cavitation phenomena occur and are of great interest, since their effect on engine performance is crucial. Zavos and Nikolakopoulos [9] have made an investigation of the cavitation deploying synthetic oils. In this investigation a commercial oil will be compared with the fullerene enhanced lubricant. The cavitation phenomena are well described and analysed by [10,11], and along with Kubota et al. [12], the Reyleigh–Plesset equations are described.

The analysis was conducted for three operation regimes of the engine [4,13] to instigate further the performance benefits of using lubricants containing fullerenes as additives. Moreover, recent investigations by Gore et al. [14] and Söderfjäll et al. [15] have emphasized on the piston ring–cylinder liner interface. It is well established that ring geometry and surface roughness play a critical role in determining lubrication performance, particularly under mixed and hydrodynamic regimes. Earlier studies [16] reported that these parameters have a great effect on the lubrication outcome, depending on the operating conditions.

The temperature range varied between 25 °C to 80 °C and the pressure was up to 2 MPa. The viscometer and its main parts are presented in Figure 1.

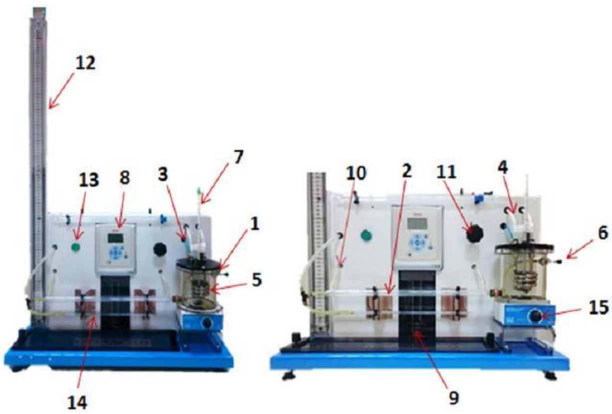

Fig. 1. The EH105 capillary tube viscometer.

The fluid under examination is introduced into the pressurized chamber (1) and secured onto the magnetic stirring device (15). Pressure is introduced into the tube (3) at a level regulated by the control valve (11) and observed using the mercury pressure gauge (12). The capillary tube is positioned within the temperature-controlled sleeve (2). Both this sleeve and the coil (5), placed inside the chamber, are supplied with water maintained at a constant temperature by the control unit (8). The fluid moves through the capillary tube at the temperature recorded by the thermometer and then flows into the calibrated pipette (14). The button (13) releases compressed air into the calibrated pipette. The chamber can be emptied via the outlet nozzle (6). By determining the time required to fill the calibrated pipette, the fluid's viscosity is calculated in relation to the temperature.

Measuring the rheological properties of a lubricant is a challenging task. The capability to assess viscosity across various flow rates, and consequently shear rates, inherently requires rheometric functionality. Viscometers such as cone and plate and coaxial cylinder ones are better suited for obtaining measurements at higher shear rates. The priority here, was given to the fullerene enhanced lubricant, which is of great interest considering that using such a lubricant, improves engine's environmental footprint in terms of emissions. The viscosity of SAE 30 is also measured, used also for validation purposes, as it had been measured previously by Nikolakopoulos et al. [4], using the same viscometer.

A two-dimensional computational fluid dynamics (CFD) model is developed using Ansys FLUENT. The flow problem is nonlinear, with the governing equations being interconnected. The pressure-based mixture model is employed, and the velocity-pressure coupling is addressed using the Semi-Implicit Method for Pressure-Linked Equations (SIMPLE) algorithm. The SIMPLE algorithm minimizes errors caused by discretization, incorporating a second-order upwind scheme. Grid sensitivity analysis tests are conducted to identify optimal mesh specifications. A grid sensitivity analysis was performed to ensure mesh independence and accuracy of the CFD model results. Multiple mesh densities were generated, ranging from coarse to highly refined quadrilateral element distributions, with the hydrodynamic pressure and film thickness profiles monitored as key output parameters. The results were compared to identify the point beyond which further mesh refinement produced negligible variation in the solution. Based on this analysis, a mesh of 31,031 quadrilateral elements was selected as the optimal configuration, balancing computational efficiency and accuracy. This grid density provided stable convergence using a time step of 10^{-3} s, with the governing equations solved via the pressure-based mixture model and the SIMPLE algorithm. The second-order upwind discretization scheme was applied to minimize numerical diffusion, and convergence was achieved when the residuals dropped below 10^{-5} for pressure. Viscosity is modeled using the power-law approach, as explained by Zavos and Nikolakopoulos [5], since the thermal transfer as the lubricant flows has been considered. The compression piston ring cylinder conjunction is presented schematically below in Figure 2.

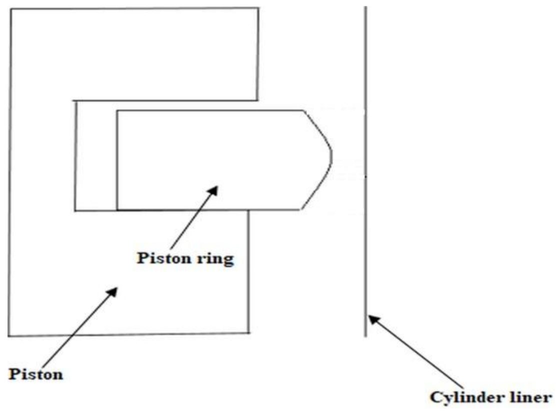

Fig. 2. Compression piston ring cylinder conjunction.

2. MEASUREMENT METHODS AND CFD MODEL

The CFD simulations were carried out on a two-dimensional domain representing the piston ring–cylinder liner conjunction, discretized into 31,031 quadrilateral elements with a corresponding number of computational nodes determined during the mesh generation stage. The grid resolution was selected after dedicated sensitivity tests to ensure that further refinement did not significantly affect predicted hydrodynamic pressures or film thickness values. All numerical work was performed using the pressure-based mixture model in ANSYS FLUENT, with the SIMPLE algorithm for velocity–pressure coupling and a time step of 10^{-3} s.

Apart from the thermal considerations, a UDF code (User Defined Function) is employed, so the asperities are regarded and affect the lubricant flow as per Greenwood and Tripp model [6]. Additionally, the cavitation phenomena are examined, trying to investigate whether and up to which area of the lubricant using fullerene additives is showing a better performance. The rheological properties of the fullerene based lubricant are well improved, as per [3].

2.1 Theory of the elastodynamics of the piston ring

The piston's sliding velocity has a vital effect on the movement of the piston. This velocity is calculated by Equation (1) as per [7]:

$$v_{ring} \approx v_p = r_{cr}\omega(\sin\varphi + \frac{\lambda_{cr}}{2}\sin2\varphi \quad (1)$$

where:

- 'r' is the radius of the crankpin.
- 'ω' is the rotational speed of the engine.
- 'φ' represents the crank angle.
- 'λ_{CR}' is the control ratio.

As explained and analysed in [4] the ring profile is considered as parabolic, with an equation of $\frac{cx^2}{(\frac{b}{2})^2}$. In reality, the ring profile has a rough axial asymmetric shape as reported in [8]. In the following Figure 3, the loads and pressures exerted on the ring are presented during both the downstroke and the upstroke. As observed, there is no change in the direction of the forces.

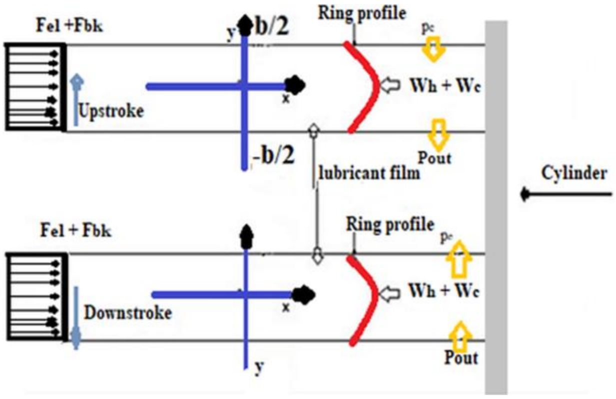

Fig. 3. Boundary conditions and forces at ring-cylinder conjunction.

However, the pressure direction changes depending on whether the piston is moving towards Top Dead Center or Bottom Dead Center.

The gas pressure at the back of the ring is determined by considering the primary forces depicted in Figure 3, which are summarized as below. Firstly, the back-gas force is given by the following equation:

$$F_G = 2\pi r_0 b_{pk}(\varphi) \quad (2)$$

Moreover, the tension force of the ring is defined as follows:

$$F_T = 2\pi b r_0 p_{el} \quad (3)$$

and the pressure due to elasticity is obtained as per Equation (4):

$$p_{el} = \frac{d_{gap} E_r \frac{bd^3}{12}}{3\pi b\left(\frac{d_{cyl}}{2}\right)^4} \quad (4)$$

where d_{gap} represents the piston-ring end gap and d_{cyl} stands for the cylinder bore diameter. In the present analysis, it is imperative that the ring tension force F_T summarized with the back-gas force F_G are balanced with the hydrodynamic reaction W_h generated by the lubricant film in the ring–liner interface, adding the load stemming from surface irregularities, denoted as W_C. The balance of the ring must be maintained at every crankshaft angle, as per the following expression:

$$F_T + F_G = W_h + W_C \quad (5)$$

In both mixed and hydrodynamic lubrication regimes, the contact in the ring-cylinder interface is not completely insulated by the film of the lubricant. Instead, a section of the ring contacts surface asperities. The local hydrodynamic capacity and the load by the surface asperities are calculated by the following equations:

$$W_h = 2\pi r_0 \int b_0 p_h dx dy \quad (6)$$

$$W_C = \frac{16\sqrt{2}}{15}\pi(\zeta\kappa\sigma)^2\sqrt{\frac{\sigma}{\kappa}}\frac{E' A F_5}{2(\lambda)} \quad (7)$$

Load balance is satisfied when Equation (8) is fulfilled:

$$X = \frac{|W(\varphi)-F(\varphi)|}{\max\{F,W\}} \leq 0.1\% \quad (8)$$

The motion of the fullerene particles as the lubricant flows in the ring-cylinder conjunction, is described by Tsakiridis and Nikolakopoulos [3]. The particles prevent the surfaces from having direct contact by rolling between them, even in the case that the lubricant film is insufficient, as in this case the lubricant is employed in mixed lubrication regime.

2.2 Method of viscosity measurements using capillary tube viscometer

The experimental procedure for the viscosity measurement of engine oils is described step by step in Figure 4. The dynamic viscosity (n) is defined as:

$$n = \frac{\Delta p}{q}\frac{\pi R^4}{8l} \quad (9)$$

where R is the capillary tube radius, l is the capillary tube length, and $\frac{\Delta p}{q}$ is the gradient from the line defined, figuring the variation of Δp versus q. All in all the procedure is well described by the flowchart in Figure 4.

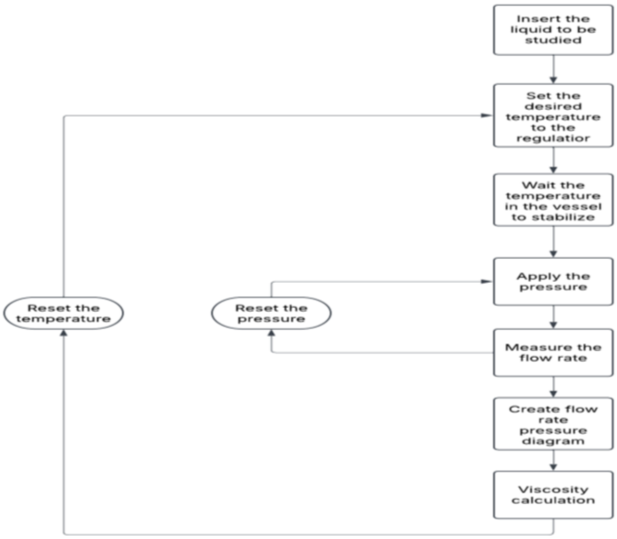

Fig. 4. The flowchart describing the viscosity measurements.

Upon receiving a set of flow rate measurements, the values were plotted against their corresponding pressures. To confirm that the flow is indeed Poiseuille flow, the experimental data points should align with a straight-line equation.

2.3 Uncertainty analysis

With respect to the procedure implemented by this device, the parameters indicated below are necessary to carry out the uncertainty assessment:

- Uncertainty in pressure measurement, $u_{\Delta p}$
- Uncertainty in flow rate measurement, u_q
- Uncertainty in volume measurement, u_v
- Uncertainty in time measurement, u_t
- Uncertainty from the radius of the capillary tube, u_r
- Uncertainty from the length of the capillary tube, u_l

Since all the above input quantities are independent, the square of the standard deviation of the output estimate is given by the following equation:

$$u^2(\eta) = \sum_{i=1}^{n} [c_i * u(x_i)]^2 = \sum_{i=1}^{n} u_i^{\,2}(\eta) \quad (10).$$

Table 1. Uncertainty parameters and their values.

Parameter(x_i)	Value u(x_i)
Δp	0.5 mm Hg
V	0.005 ml
T	0.01 s
L	0.0025 mm
R	0.05 mm

The uncertainty equation is:

$$u^2(\eta) = \sum \left(\frac{\theta\eta}{\theta(\Delta p)} u(\Delta p) + \frac{\theta\eta}{\theta(V)} u(V) + \frac{\theta\eta}{\theta(t)} u(t) + \frac{\theta\eta}{\theta(l)} u(l) + \frac{\theta\eta}{\theta(R)} u(R) \right)^2 =$$

$$\sum \left(\frac{\pi\, R^4}{q\, 8\, l} \mathrm{u}(\Delta p) - \frac{\Delta p\, \pi\, R^4 t}{8\, l} \frac{1}{V^2} u(V) + \frac{\Delta p\, \pi\, R^4}{V\, 8\, l} u(t) + \frac{\Delta p\, \pi\, R^3}{q\, 2\, l} u(R) - \frac{\Delta p\, \pi\, R^4}{q\, 8\, l^2} u(l) \right)^2 \quad (11)$$

And by calculating for all the measurements taken at different temperatures and pressures, we conclude that:

$$u^2(\eta) = 0{,}001698167$$

The combined uncertainty is derived from the positive square root of the variance:

$$u_c(\eta) = \sqrt{u_\eta^{\,2}} = 0{,}041208$$

The uncertainty assigned to each result should be of an appropriate range so that it covers an interval with a high degree of confidence (increasing the probability of the result's correctness). As a result,

$$U = k * u_c(y) = 2 * 0{,}041208 = 0{,}082416$$

2.4 Cavitation model analysis

The CFD model of the lubricant flow is deployed using ANSYS FLUENT, considering thermal transfer between the surfaces and the lubricant, the Greenwood-Tripp model and the cavitation phenomena as well.

Cavitation arises when, at a specified temperature, the local pressure within a liquid stream falls below the corresponding saturated vapor pressure [9]. This phenomenon is frequently encountered in piston rings during motion reversals, particularly at both top and bottom dead center (TDC, BDC), and, under certain operating conditions, at the mid-stroke position. The present analysis incorporates liquid–vapor mass transfer mechanisms, including cavitation, which are modeled through the following vapor transport equation [10].

$$\frac{\partial(a_v\rho_v)}{\partial t} + \nabla\cdot\left(a_v\rho_v\overrightarrow{V_u}\right) = R_e - R_c \qquad (12)$$

Here, ρ_v denotes the vapor density, and V_u represents the velocity vector of the vapor phase. The terms R_e and R_c correspond to the mass transfer rates associated with vapor bubble growth and collapse, respectively. The evolution of these bubbles is determined using the Rayleigh–Plesset equation, which models the dynamics of a single vapor bubble within a liquid and yields the rate expressions governing vapor generation and condensation.

$$R_b\frac{d^2R_b}{dt^2} + \frac{3}{2}\left(\frac{d^2R_b}{dt}\right)^2 + \frac{2\cdot\sigma}{\rho_f R_b} = \frac{p_{sat}-p}{\rho_f} \qquad (13)$$

Furthermore, Singhal et al. [11] demonstrated that the working fluid comprises a mixture of vapor and liquid phases. They proposed a modified form of the governing equation, expressed in terms of the vapor mass fraction f_{mass}, as follows:

$$\frac{\partial(f_{mass}\rho_m)}{\partial t} + \nabla\cdot\left(f_{mass}\rho_m\overrightarrow{V_u}\right) = \nabla\cdot(\nabla f_{mass}\Gamma) + R_e - R_c \qquad (14)$$

where ρ_m corresponds to the mixture density, and Γ to the diffusion coefficient. Mass transfer rates are evaluated through the Rayleigh–Plesset equations, which consider the constraints imposed by finite bubble sizes (interface surface area per unit vapor volume). The rates vary with the instantaneous local pressures and are defined as follows:

$$R_e = C_e\frac{Vc\dot{h}}{\sigma z}\rho_l\rho_u\sqrt{\frac{2(p-p_{sat})}{3\rho_l}}f_{mass}, \quad for\ p > p_{sat} \qquad (15)$$

$$R_e = C_c\frac{Vc\dot{h}}{\sigma z}\rho_l\rho_u\sqrt{\frac{2(p_{sat}-p)}{3\rho_l}}(1-f_{mass}), \quad for\ p > p_{sat} \qquad (16)$$

Here, l and u correspond to the liquid and vapor phases, respectively. p_{sat} is the saturation vapor pressure of the liquid at the specified temperature, $Vc\dot{h}$ represents a characteristic velocity, σz denotes the surface tension of the liquid, and the empirical constants C_eC_c are set to 50 and 0.01 in accordance with Kubota et al. [12].

The cavitation phenomena were modelled deploying two phases as a mixture, the liquid and the vapor phase, and the fullerenes were deployed by using the discrete phase model. With this model the liquid-vapor mixture is homogenous but, on the other hand, the lubricant-fullerenes mixture is non-homogenous. In Table 2 the parameters of the cavitation model are presented.

Table 2. Cavitation parameters for the CFD model.

Parameter	Symbol	Units	Value
Vaporization Pressure	P_v	Pa	$2*10^4$
Atmospheric Pressure	P_{atm}	Pa	101.325
Lubricant density in vapor phase	ρ_g	Kg/m^3	1,2
Bubble's diameter	D_b	m	$2*10^{-5}$
Lubricant viscosity in vapor phase	μ_g	Pas	10^{-5}

These values for the cavitation model used for the analysis, while the lubricant used is SAE 30. The lubricant properties are well described and analysed by Zavos [9]. This research was used for validation of the results obtained from this model.

The piston ring speed as well as the chamber pressure, for every angle of the crankshaft, are used as boundary conditions in our CFD model. This analysis investigates the performance of the two lubricants under three operation regimes of an engine.

1. 1500 rpm 50% throttle
2. 1500 rpm 100% throttle
3. 2500 rpm 100% throttle

Piston ring velocity for an engine operating at these three regimes is presented, as well as the chamber pressure for every crank angle are presented in [4,13].

Throttle percentage refers to the position of the butterfly valve within the throttle body, as shown in Figure 5, which regulates the intake airflow. This parameter is critical for controlling engine performance, not only in carbureted systems but also in modern fuel-injected engines.

Fig. 5. Throttle percentage and butterfly.

In order to further analyze the way the throttle percentage affects the system, the following figure is of great interest. Figure 6 illustrates the throttle position variation as a function of crankshaft angle, indicating that under higher load conditions, the throttle remains more consistently open, which directly leads to increased air intake and higher in-cylinder pressures.

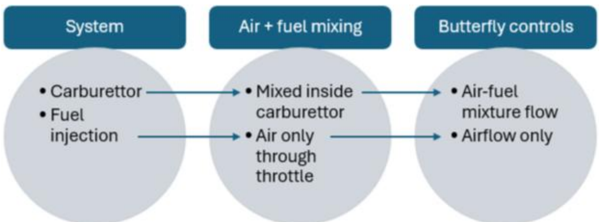

Fig. 6. Carburettor and injection system analysed.

Recent research by Gore et al. [14] and Söderfjäll et al. [15] has significantly focused on analyzing the piston ring interface, integrating numerical predictions with well-validated direct measurements. Notably, the geometry and surface roughness of the ring can significantly affect lubrication mechanisms, especially in mixed and hydrodynamic regimes. Previous studies [16] have demonstrated that these effects can vary by 5–25%, depending on operational conditions. The key contribution of this study is its exploration of how nanoparticle-enhanced lubricants influence this system, utilizing an advanced CFD model to deepen our understanding of this intricate interaction.

Geometry of the top compression ring and cylinder with representative lubrication conditions is presented in Figure 7. The contact zones are identified as follows: (a–b) fully lubricated, (b–c) cavitating, and (c–d) reformed lubricant film.

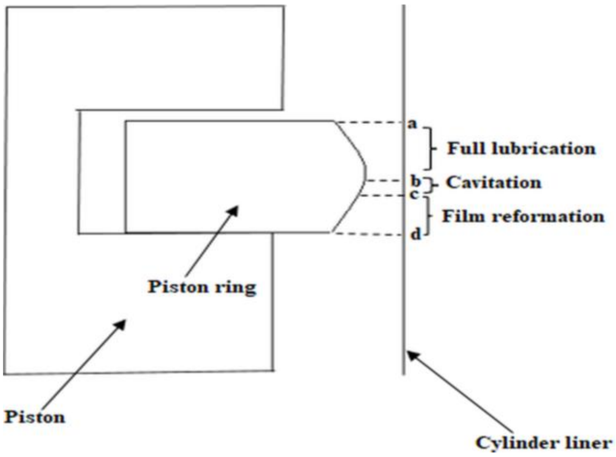

Fig. 7. A 2D schematic of the compression ring–cylinder conjunction indicating lubrication behavior across the domain: a–b) fully lubricated region, (b–c) cavitation zone, and (c–d) reformation of the oil film.

3. RESULTS

3.1 Capillary tube viscometer results

Before measuring the viscosity of the lubricant using fullerene additives it was crucial to validate the results obtained. Therefore, firstly the procedure was done for SAE 30 lubricant, at 60 °C, 70 °C and 75 °C, and the viscosity values were compared to Nikolakopoulos et. al [4], and the divergence was negligible. Following the procedure was done for the fullerene lubricant and the relevant results are presented below. The pressure was set to 100 mmHg, 200 mmHg and 300 mmHg respectively.

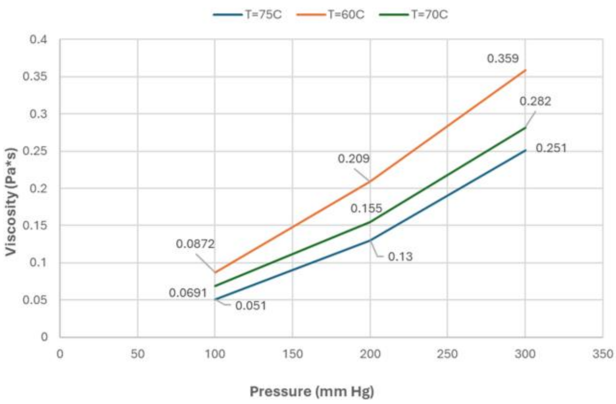

Fig. 8. Viscosity of fullerene lubricant at various pressures and temperatures.

As shown in Figure 8, viscosity decreases as temperature increases, which is consistent with expected behavior. Additionally, pressure has a significant influence on viscosity; as pressure rises, viscosity also increases. To highlight the critical role of fullerenes in enhancing the rheological properties of the lubricant, Figure 9 below presents viscosity curves of a conventional SAE 30 lubricant.

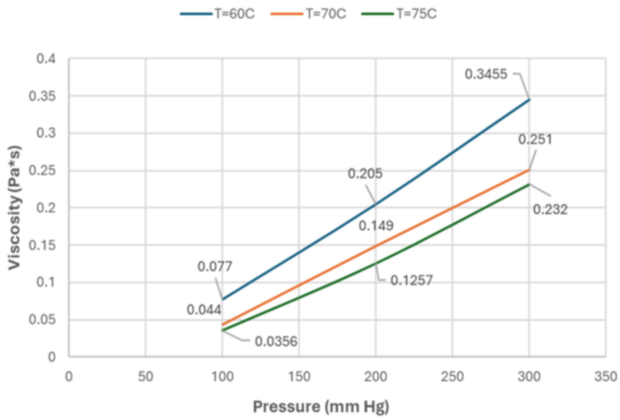

Fig. 9. Viscosity of SAE 30 lubricant at various pressures and temperatures.

The viscosity of the lubricant containing fullerenes as additives increases and maintains its properties even as the temperature rises. While viscosity typically decreases with increasing temperature, the fullerene-enhanced lubricant demonstrates significantly less degradation compared to conventional monograde oil. This is a critical advantage, as engines often operate under high-temperature conditions, and maintaining sufficient lubricant viscosity, is essential for optimal engine performance and protection.

3.2 Cavitation model results

By using the CFD model a study of the tribological performance of the two lubricants was done, considering the cavitation and computing the volume of fraction of the vapor phase.

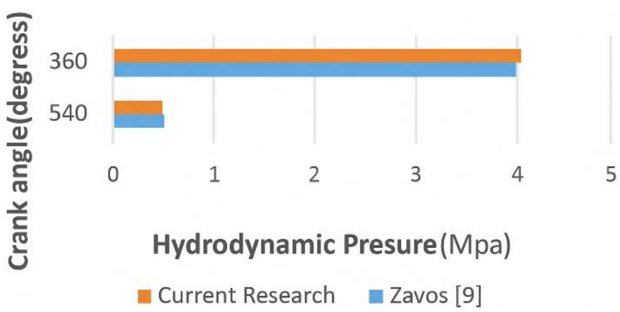

Fig. 10. Validation diagram.

For the validation of the results, before proceeding to the investigation, there were used the boundary conditions described in [9], and the results obtained were compared. In Figure 10 the validation diagram is presented.

The hydrodynamic pressure is computed at two different angles, -180° and 360° of the crankshaft and the difference is predicted up to 3%. Therefore, the results are robust, and the investigation is proceeding further for the fullerenes lubricant. The results obtained for the lubricant containing fullerenes are compared with the ones for the SAE 30. The results obtained in terms of hydrodynamic pressure and volume fraction of the vapor phase are presented and analysed.

In the following figures, there is a comparison between the hydrodynamic pressure exerting on the piston ring at -180°, as the two lubricants flow, for the three operating regimes of an engine.

Figures 11–13 show an increase in pressure when fullerene oil is used. This outcome is expected under mixed lubrication conditions, where thinner lubricant films typically result in increased hydrodynamic pressure. The lubricant containing fullerenes results in thinner lubricant films, as reported in [3], since the particles enhance the rheological properties of the lubricant. Additionally, at as the rpm or the throttle increases, the hydrodynamic pressure increases, for both lubricants, the monograde SAE 30 and the lubricant containing fullerenes as additives.

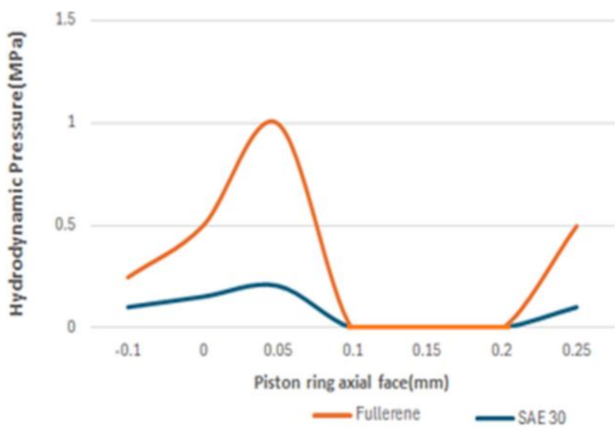

Fig. 11. Hydrodynamic pressure at -180° for the two lubricants along the piston ring profile at 1500 rpm and 50% throttle.

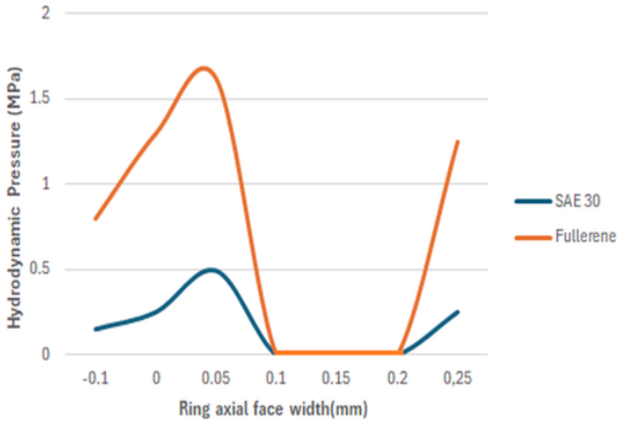

Fig. 12. Hydrodynamic pressure at -180° for the two lubricants along the piston ring profile at 1500 rpm and 100% throttle.

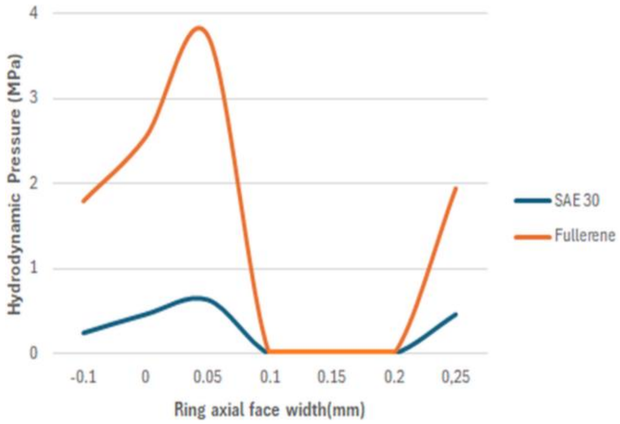

Fig. 13. Hydrodynamic pressure at -180° for the two lubricants along the piston ring profile at 2500 rpm and 100% throttle.

In the following figures there will be a comparison of the hydrodynamic pressure exerting on the piston ring at 360°, for the two lubricants, at the three engine operation regimes.

At ϕ = 360°, during the downstroke, the contact area shrinks. Yet, in Figures 14-16 it is illustrated that fullerene oil maintains higher pressure levels, indicating its ability to sustain lubrication under various conditions. More specifically, the pressure is increased when the fullerene oil is deployed. In mixed lubrication regime, where the thinner lubricant film causes increased hydrodynamic pressure, this is expected. The lubricant containing fullerenes corresponds to lower lubricant films as per [3], since the particles enhance the rheological properties of the lubricant.

In the following figures the same comparison, in terms of volume fraction, is presented at both crank angles. At -180° the piston is near the Top Dead Center, but at 360° it is near the Bottom Dead Center, so another comparison can be done of how the two lubricants correspond at these two different positions.

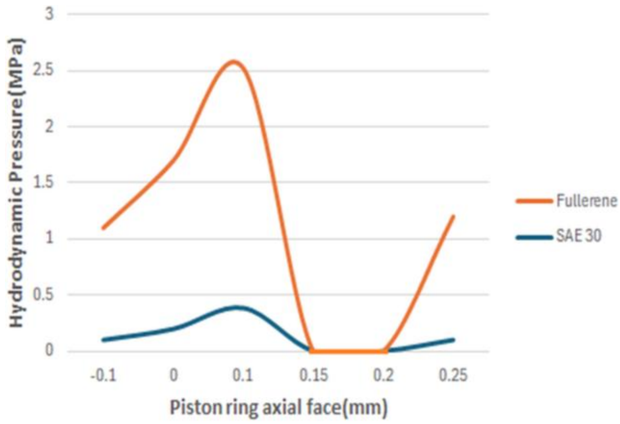

Fig. 14. Hydrodynamic pressure at 360° for the two lubricants along the piston ring profile at 1500 rpm and 50% throttle.

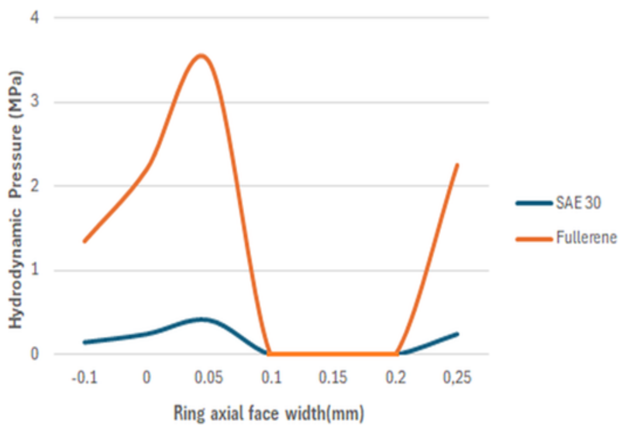

Fig. 15. Hydrodynamic pressure at 360° for the two lubricants along the piston ring profile at 1500 rpm and 100% throttle.

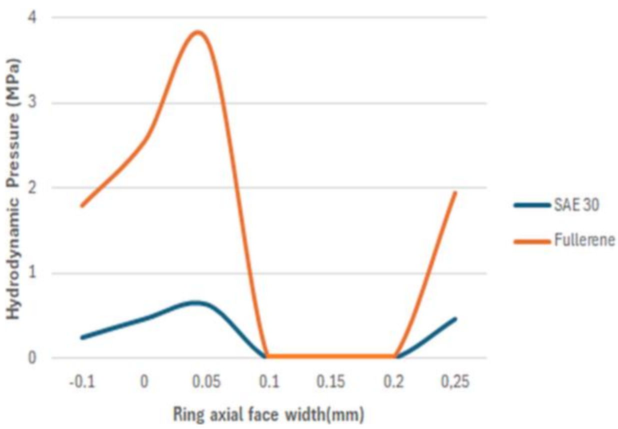

Fig. 16. Hydrodynamic pressure at 360° for the two lubricants along the piston ring profile at 2500 rpm and 100% throttle.

Figures 17–22 clearly demonstrate that as engine load increases, the volume fraction of the vapor phase also increases, regardless of the lubricant used. The increase in vapor volume fraction from case 1 to cases 2 and 3 is due to the higher engine loads and speeds, which raise local shear and reduce lubricant film thickness. This promotes localized pressure drops below the vaporization limit, leading to more intense cavitation and therefore a higher volume of fraction. As shown in Figures 17,19 and 21 when the fullerene enhanced oil is used, the vapor phase is less affected, since the contours show minimal deviation and the maximum values have negligible differences. When the operating condition changes from 1500 rpm 50% throttle to 1500 rpm 100% throttle the vapor volume of fraction increases about 0,70%, while when changing from 1500 rpm 100% throttle to 2500 rpm 100% throttle the increase is about 0,60%. On the other hand, for the monograde SAE 30 at Figures 18,20 and 22 the volume fraction is increased significantly, particularly near the piston ring area. More specifically, the volume of fraction increases by about 3,2% when the operating condition changes from 1500 rpm 50% throttle to 1500 rpm 100% throttle, and 0,50 % when changing from 1500 rpm 100% throttle to 2500 rpm 100% throttle respectively.

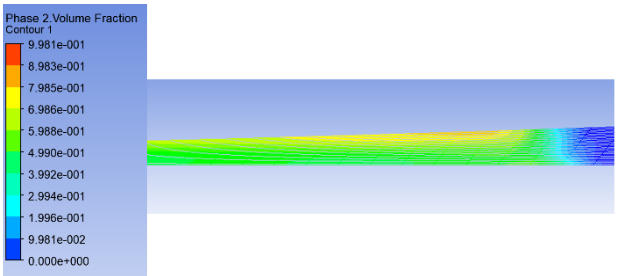

Fig. 17. Volume of fraction of the vapor phase at -180° for the fullerene lubricant at 1500 rpm and 50% throttle.

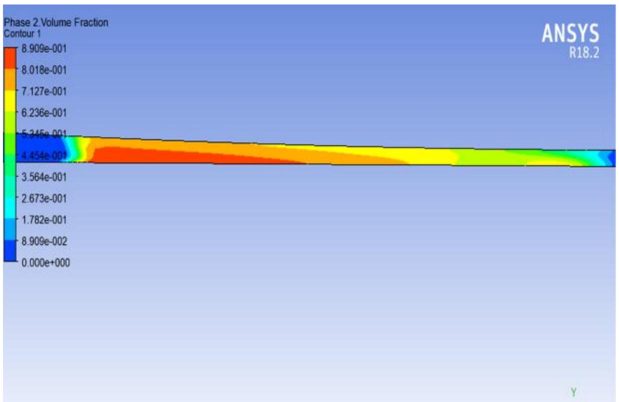

Fig. 18. Volume of fraction of the vapor phase at -180° for the SAE 30 lubricant at 1500 rpm and 50% throttle.

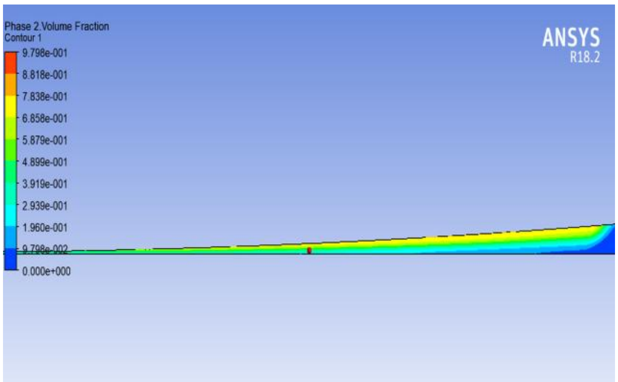

Fig. 19. Volume of fraction of the vapor phase at -180° for the fullerene lubricant at 1500 rpm and 100% throttle.

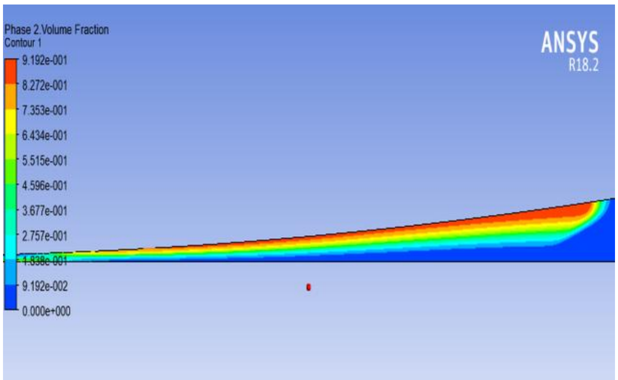

Fig. 20. Volume of fraction of the vapor phase at 360° for the SAE 30 lubricant at 1500 rpm and 100% throttle.

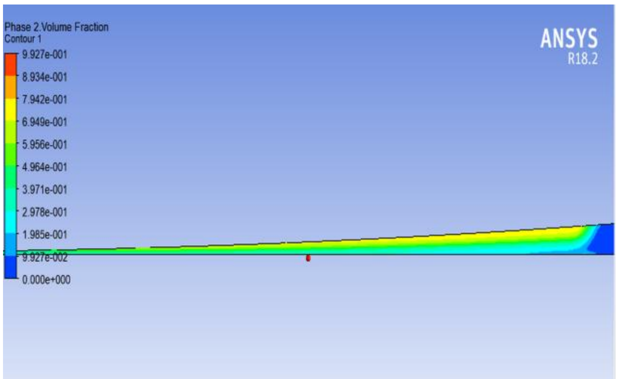

Fig. 21. Volume of fraction of the vapor phase at -180° for the fullerene lubricant at 2500 rpm and 100% throttle.

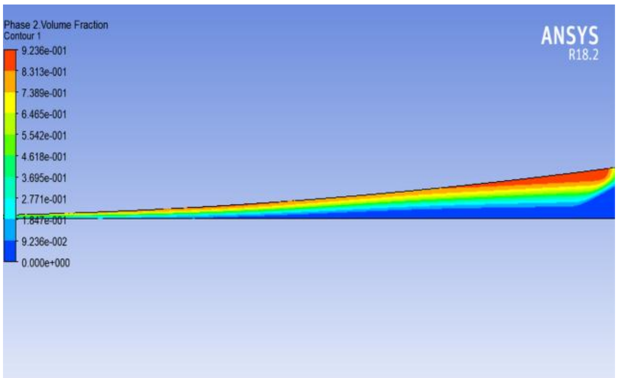

Fig. 22. Volume of fraction of the vapor phase at -180° for the SAE 30 lubricant at 2500 rpm and 100% throttle.

The above figures show the volume fraction of the vapor phase for the two lubricants near TDC, but it crucial to observe how the two lubricants perform near the BDC.

Figures 23-28 highlight the influence of load increasing to the vapor volume of fraction near BDC. For the monograde SAE 30 when the operating condition changes from 1500 rpm 50% throttle to 1500 rpm 100% throttle the volume of fraction increases by about 8.5%, while when changing from 1500 rpm 100% throttle to 2500 rpm 100% throttle the volume of fraction indicates an increase of 5.5%. When the fullerene oil is deployed the volume of fraction increases 0,8% and 0.7% respectively.

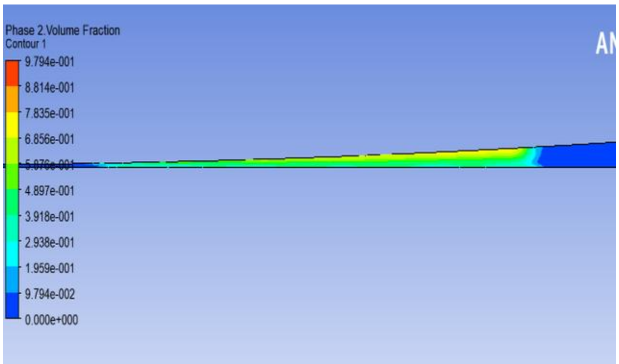

Fig. 23. Volume of fraction of the vapor phase at 360° for the fullerene lubricant at 1500 rpm and 50% throttle.

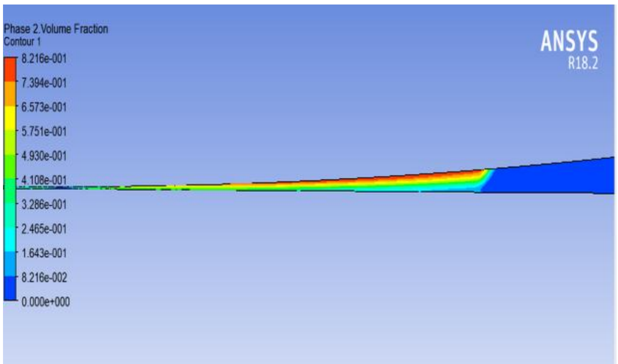

Fig. 24. Volume of fraction of the vapor phase at 360° for the SAE 30 lubricant at 1500 rpm and 50% throttle.

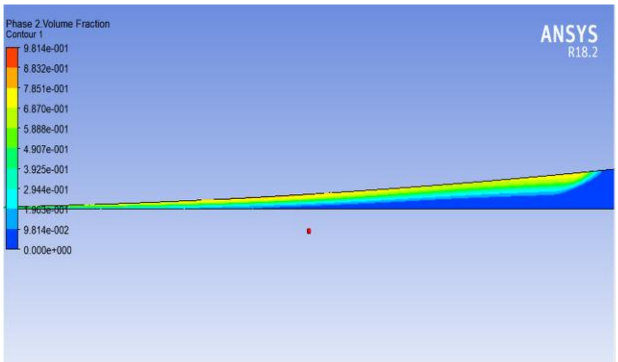

Fig. 25. Volume of fraction of the vapor phase at 360° for the fullerene lubricant at 1500 rpm and 100% throttle.

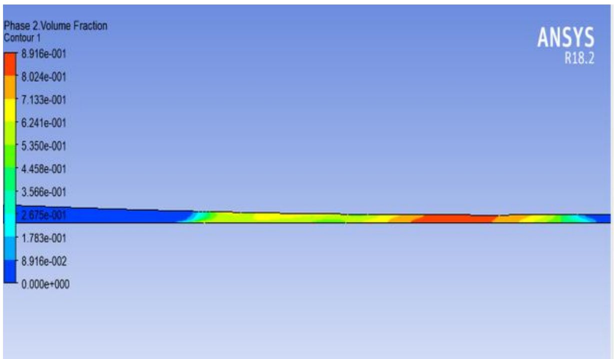

Fig. 26. Volume of fraction of the vapor phase at 360° for the SAE 30 lubricant at 1500 rpm and 100% throttle.

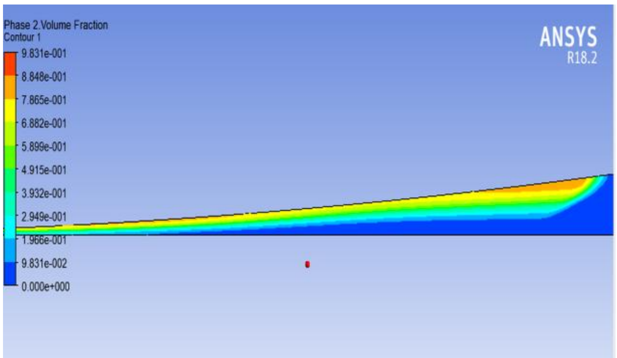

Fig. 27. Volume of fraction of the vapor phase at 360° for the fullerene lubricant at 2500 rpm and 100% throttle.

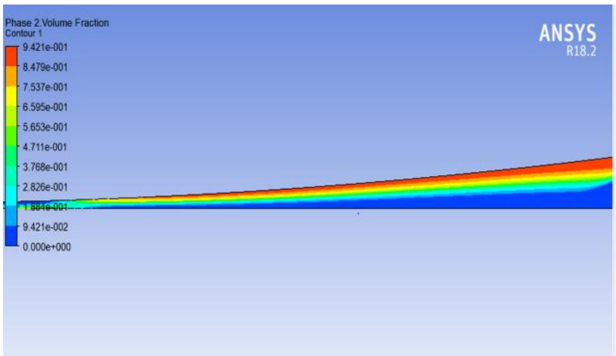

Fig. 28. Volume of fraction of the vapor phase at 360° for the SAE 30 lubricant at 2500 rpm and 100% throttle.

In Figure 29 these differences are shown in a bar chart, where the vapor volume of fraction of the vapor phase is shown for the three operation regimes and for the two angles of the crankshaft for both lubricants.

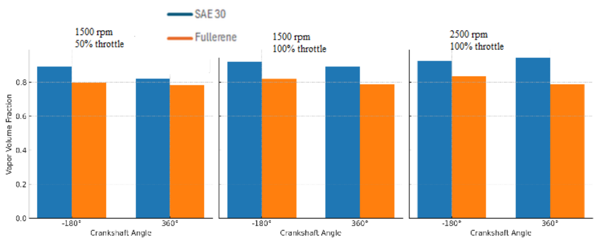

Fig. 29. Comparison of the vapor volume of fraction at the three operating regimes of the engine at -180° and 360° for the SAE 30 and the fullerene oil.

As observed at every angle and at every operation regime when the lubricant containing fullerenes as additives is deployed the volume of fraction is well reduced.

The figures above illustrate the hydrodynamic pressures that are generated, along with the vapor volume fraction , during the stroke reversals. It is clear that under high load and low speed conditions, particularly during the transition from the compression to the power stroke near top dead center (TDC), the contact area between the ring profile and the cylinder liner has been expanded. This occurs because the ring moves upward slowly at TDC (ϕ = -180°). Conversely, as the piston moves downward after the power stroke and approaches bottom dead center (BDC) (ϕ = 360°), the contact area of the ring reduces. This reduction is due to the lower load and the presence of an adequate minimum film thickness, supported by higher lubricant viscosity under isothermal conditions. The cavitation intensity is significantly reduced when the lubricant containing fullerenes is deployed, at both angles and at every operation regime. This highlights the performance benefits when these lubricants are used. The phase change rate depends on the flow conditions and the fluid properties, as per [17]. Reducing cavitation isn't just about smoother lubrication, it's a leap towards longer-lasting engines, higher efficiency, and more sustainable performance.

Additionally, the friction force is of great interest, and Figures 30-32 illustrate the vital role that fullerenes play in improving the properties of the lubricant. Although the hydrodynamic pressure is increased, the friction is significantly reduced. The decreased friction results also in decreased wear volume and further to higher engine efficiency and potential reduction in emissions.

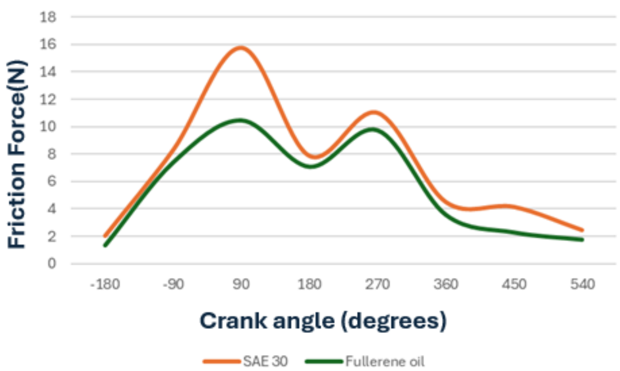

Fig. 30. Viscous friction of lubricant SAE 30 and the lubricant containing fullerenes at 1500 rpm 50% throttle.

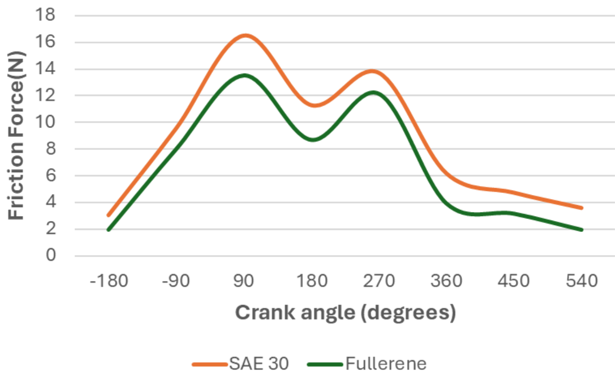

Fig. 31. Viscous friction of lubricant SAE 30 and the lubricant containing fullerenes at 1500 rpm 100% throttle.

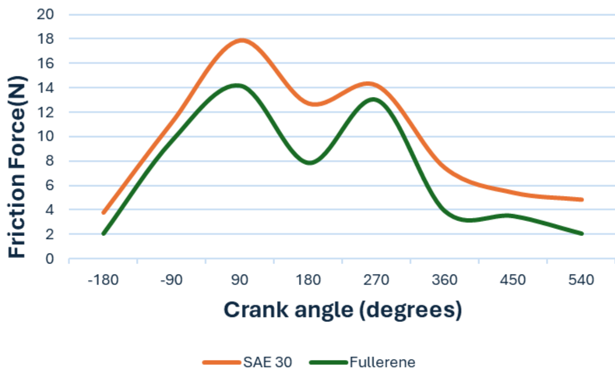

Fig. 32. Viscous friction of lubricant SAE 30 and the lubricant containing fullerenes at 2500 rpm 100% throttle.

Figures 30-32 clearly illustrate the advantages of using fullerene-enhanced lubricants over conventional oils. The friction force is consistently lower at every crankshaft angle and under all engine operating regimes. This confirms the beneficial impact of fullerene nanoparticles on reducing friction and improving lubrication efficiency.

Friction remains a critical factor influencing both fuel efficiency and the lifetime of internal combustion (IC) engines, particularly given the vast number of vehicles in the global transportation sector [18]. Light-duty vehicles account for the majority of energy consumption (approximately 52%), followed by trucks (17%), marine vessels (10%), aviation (10%), and buses (4%). A comprehensive analysis by Holmberg et al. [19] highlighted that parasitic frictional losses are most significant in engines and transmissions, comprising about 15–20% of total engine losses. Notably, nearly 45% of these losses originate from the piston assembly. Within this assembly, the ring-pack—especially the top compression ring—is the dominant source of friction, contributing between 13% and 40% depending on engine type and operating conditions, as reported by Richardson et al. [20].

Of great interest is the performance of fullerene particle under high temperatures. Whether an engine is operating properly, temperature shall not exceed 90-100°C. But in case of failure, it is crucial to estimate how the fullerene particle performs. Complementing these tribological findings, thermal analysis of C_{60}-based polymers shows that the fullerene cage remains structurally intact at temperatures up to ~670 °C. Degradation initiates only in the organic side chains well above typical engine operating temperatures, underscoring the high thermal stability of the carbon cage [21]. While such polymers differ structurally from nanoparticle dispersions, this reveals the fundamental heat resistance of fullerenes, further supporting their potential for high-temperature lubrication applications. In the presence of oxygen (e.g., air), C60 decomposition can start around 440-725 °C [21]. In inert atmospheres (like nitrogen), the decomposition temperature can be higher, potentially around 670 °C or even 700 °C and beyond [22].

4. CONCLUSIONS

A CFD model is developed to study the effect of lubricants containing fullerenes against SAE 30 lubricant oils, regarding the tribology of the piston ring problem, under engine representative conditions. The results confirm that fullerenes significantly improve the rheological properties of the lubricant. These improvements include increased viscosity stability under varying shear rates and temperatures, as well as enhanced load-bearing capacity, which can contribute to reduced friction and wear in tribological applications. In terms of hydrodynamic pressure, the lubricant containing fullerenes as additives corresponds to higher values of pressure. The minimum film thickness is well decreased when the fullerene oil is deployed as per [3], and so the hydrodynamic pressure is increased by almost 70% at -180° and by almost 80% at 360**.** The increase in hydrodynamic pressure results from the thinner lubricant film observed when fullerene-enhanced oil is used—particularly under mixed lubrication conditions [3,5,9]. On the other hand, friction force decreases by almost 35% at its maximum value at 90^0 at 1500 rpm and 50% throttle, while the maximum decrease at 1500 rpm 100% throttle is indicated at 270^0 and is about 36%. At the same time at 2500 rpm and 100% throttle the maximum decrease is observed at 270^0 and is about 47%.

The experimentally measured viscosity indicates that the lubricant containing fullerenes as additives exhibits significantly improved performance, since the fullerenes indeed enhance the rheological properties of the lubricant [3]. Unlike lubricant SAE 30, the viscosity of fullerene enhanced lubricant remains more stable as the temperature increases, demonstrating a higher viscosity index, as per Figure 5. More specifically, for pressure 100 mmHg the viscosity of SAE 30 when the temperature rises from 60 °C to 70 °C indicates a decrease of 42%, while the fullerene oil only 20%. Additionally, for 300 mmHg pressure, when the temperature follows the same increase, the decrease of viscosity is 27% for SAE 30 and 21% for fullerene oil. This also highlights the great influence of fullerene particles, since the decrease in viscosity is almost the same for the two pressure regimes while for SAE 30 the decrease is way higher at low pressure. Furthermore, the fullerene-based lubricant not only performs better with temperature variations but also maintains superior stability under pressure changes. The maximum increase is obtained for both lubricants, for temperature of 70 °C. Specifically, SAE 30 increases its viscosity when the pressure increases from 100 mmHg to 200 mmHg by about 70%. Respectively, the viscosity of the fullerene oil increases 55% at the same time. The maximum difference in viscosity values between the two lubricants is obtained at 70 °C and pressure 100 of mmHg, which is about 35%.

REFERENCES

[1] H. Spikes, "Friction modifier additives," *Tribology Letters*, vol. 60, no. 1, Sep. 2015, doi: 10.1007/s11249-015-0589-z.

[2] L. R. Rudnick, *Lubricant Additives: Chemistry and applications*. 2007. doi: 10.1201/9781315120621.

[3] E. Tsakiridis and P. Nikolakopoulos, "Fullerene Oil Tribology in Compression Piston Rings under Thermal Considerations," *Lubricants*, vol. 11, no. 12, p. 505, Nov. 2023, doi: 10.3390/lubricants11120505.

[4] P. G. Nikolakopoulos, S. Mavroudis, and A. Zavos, "Lubrication Performance of Engine Commercial Oils with Different Performance Levels: The Effect of Engine Synthetic Oil Aging on Piston Ring Tribology under Real Engine Conditions," *Lubricants*, vol. 6, no. 4, p. 90, Oct. 2018, doi: 10.3390/lubricants6040090.

[5] A. Zavos and P. G. Nikolakopoulos, "A tribological study of piston rings lubricated by power law oils," *Proceedings of the Institution of Mechanical Engineers Part J Journal of Engineering Tribology*, vol. 230, no. 5, pp. 506–524, Sep. 2015, doi: 10.1177/1350650115606481.

[6] J. A. Greenwood and J. H. Tripp, "The contact of two nominally flat rough surfaces," *Proceedings of the Institution of Mechanical Engineers*, vol. 185, no. 1, pp. 625–633, Jun. 1970, doi: 10.1243/pime_proc_1970_185_069_02.

[7] C. Baker, S. Theodossiades, R. Rahmani, H. Rahnejat, and B. Fitzsimons, "On the Transient Three-Dimensional Tribodynamics of Internal Combustion Engine Top Compression Ring," *Journal of Engineering for Gas Turbines and Power*, vol. 139, no. 6, Nov. 2016, doi: 10.1115/1.4035282.

[8] W. Ma, N. Biboulet, and A. A. Lubrecht, "Performance evolution of a worn piston ring," *Tribology International*, vol. 126, pp. 317–323, May 2018, doi: 10.1016/j.triboint.2018.05.028.

[9] A. Zavos and P. G. Nikolakopoulos, "Cavitation effects on textured compression rings in mixed lubrication," *Lubrication Science*, vol. 28, no. 8, pp. 475–504, May 2016, doi: 10.1002/ls.1341.

[10] I. Senocak and W. Shyy, "Interfacial dynamics-based modelling of turbulent cavitating flows, Part-1: Model development and steady-state computations," *International Journal for Numerical Methods in Fluids*, vol. 44, no. 9, pp. 975–995, Mar. 2004, doi: 10.1002/fld.692.

[11] A. K. Singhal, M. M. Athavale, H. Li, and Y. Jiang, "Mathematical basis and validation of the full cavitation model," *Journal of Fluids Engineering*, vol. 124, no. 3, pp. 617–624, Aug. 2002, doi: 10.1115/1.1486223.

[12] A. Kubota, H. Kato, and H. Yamaguchi, "A new modelling of cavitating flows: a numerical study of unsteady cavitation on a hydrofoil section," *Journal of Fluid Mechanics*, vol. 240, pp. 59–96, Jul. 1992, doi: 10.1017/s002211209200003x.

[13] R. Rahmani, H. Rahnejat, B. Fitzsimons, and D. Dowson, "The effect of cylinder liner operating temperature on frictional loss and engine emissions in piston ring conjunction," *Applied Energy*, vol. 191, pp. 568–581, Feb. 2017, doi: 10.1016/j.apenergy.2017.01.098.

[14] M. Gore, R. Rahmani, H. Rahnejat, and P. King, "Assessment of friction from compression ring conjunction of a high-performance internal combustion engine: A combined numerical and experimental study," *Proceedings of the Institution of Mechanical Engineers Part C Journal of Mechanical Engineering Science*, vol. 230, no. 12, pp. 2073–2085, May 2015, doi: 10.1177/0954406215588480.

[15] M. Söderfjäll, A. Almqvist, and R. Larsson, "Component test for simulation of piston ring – Cylinder liner friction at realistic speeds," *Tribology International*, vol. 104, pp. 57–63, Sep. 2016, doi: 10.1016/j.triboint.2016.08.021.

[16] M. Kennedy, S. Hoppe, and J. Esser, "Lower friction losses with new Piston ring coating," *MTZ Worldwide*, vol. 75, no. 4, pp. 24–29, Mar. 2014, doi: 10.1007/s38313-014-0135-7.

[17] A. K. Singhal, M. M. Athavale, H. Li, and Y. Jiang, "Mathematical basis and validation of the full cavitation model," *Journal of Fluids Engineering*, vol. 124, no. 3, pp. 617–624, Aug. 2002, doi: 10.1115/1.1486223.

[18] World Energy Council, Ed., *Global transport scenarios 2050*. London, UK: World Energy Council, 2011. [Online]. Available: https://www.worldenergy.org/assets/downloads/wec_transport_scenarios_2050.pdf

[19] K. Holmberg, P. Andersson, and A. Erdemir, "Global energy consumption due to friction in passenger cars," *Tribology International*, vol. 47, pp. 221–234, Dec. 2011, doi: 10.1016/j.triboint.2011.11.022.

[20] D. E. Richardson, "Review of power cylinder friction for diesel engines," *Journal of Engineering for Gas Turbines and Power*, vol. 122, no. 4, pp. 506–519, Apr. 2000, doi: 10.1115/1.1290592.

[21] G. Lisa, C. Cleminte, and T. Michinobu, "Thermal stability and degradation mechanism of C60 fullerene-based polymers," *Journal of Applied Polymer Science*, vol. 141, no. 11, Dec. 2023, doi: 10.1002/app.55079.

[22] C. S. Sundar, A. Bharathi, Y. Hariharan, J. Janaki, V. S. Sastry, and T. S. Radhakrishnan, "Thermal decomposition of C60," *Solid State Communications*, vol. 84, no. 8, pp. 823–826, Nov. 1992, doi: 10.1016/0038-1098(92)90098-t.